

Simulating open quantum dynamics on an NMR quantum processor using the Sz.-Nagy dilation algorithm

Akshay Gaikwad,^{*} Arvind,[†] and Kavita Dorai[‡]

*Department of Physical Sciences, Indian Institute of Science Education & Research Mohali,
Sector 81 SAS Nagar, Manauli PO 140306 Punjab India.*

We experimentally implement the Sz.-Nagy dilation algorithm to simulate open quantum dynamics on an nuclear magnetic resonance (NMR) quantum processor. The Sz.-Nagy algorithm enables the simulation of the dynamics of arbitrary-dimensional open quantum systems, using only a single ancilla qubit. We experimentally simulate the action of two non-unitary processes, namely, a phase damping channel acting independently on two qubits and a magnetic field gradient pulse (MFGP) acting on an ensemble of two coupled nuclear spin-1/2 particles. To evaluate the quality of the experimentally simulated quantum process, we perform convex optimization-based full quantum process tomography to reconstruct the quantum process from the experimental data and compare it with the target quantum process to be simulated.

I. INTRODUCTION

In 1982, Richard Feynman proposed the idea of simulating quantum systems using a universal quantum computer [1], which received a lot of attention from the scientific community [2–4]. Over the following decades, this led to efforts to build quantum computers which could solve computational problems exponentially faster, as compared to their classical counterparts [5]. The main building block of a quantum computer is the underlying physical system and its time evolution under a given Hamiltonian [6], while the main obstacle in building such a quantum computer is its unwanted and inevitable interaction with its environment, generally referred to as decoherence [7]. This led to studies of open quantum dynamics, whereby the time evolution of a quantum system was studied using different approaches [8, 9].

The physical implementation of quantum algorithms mostly relies on unitary quantum gates. However, in real situations, the physical system under consideration is continuously interacting with its environment, causing its time evolution to be non-unitary. In some cases, the noise from open dynamics can contribute significantly to errors in the computational output, leading to lower experimental fidelity and a reduction in the quality of the quantum device [10]. A duality quantum algorithm for simulating Hamiltonian evolution of an open quantum system was proposed where the time evolution is realized using Kraus operators [11, 12]. A quantum algorithm was proposed to simulate a general finite-dimensional Lindblad master equations without needing to engineer system-environment interactions [13]. A method for efficient quantum simulation of open quantum dynamics for various Hamiltonians and spectral densities was recently proposed [14].

Several techniques have been proposed to simulate spe-

cific types of quantum channels and have been experimentally realized using different physical platforms. A control technique to drive an open quantum system from the Markovian to the non-Markovian regime was demonstrated on an optical setup [15]. A model was designed that precisely controls the strength of non-Markovian effects by changing the degree of correlation and qubit-environment interaction time on an NMR system [16]. Non-positive dynamical maps the decoherence dynamics of a qubit were experimentally demonstrated using photons [17]. A technique to simulate Markovian and non-Markovian dynamics was proposed on a cavity-QED setup [18]. Multiqubit open dynamics was simulated on an IBM quantum processor for several quantum processes including unital and non-unital dynamics as well as Markovian and non-Markovian evolution [19]. A dilation procedure was employed to simulate non-hermitian Hamiltonian dynamics using ancilla qubits [20].

Recently, promising quantum algorithms to simulate arbitrary non-unitary evolutions on quantum devices have been reported, which are primarily based on the dilation technique namely, the Stinespring dilation algorithm [21] and Sz.-Nagy's dilation algorithm [22]. The basic tenet of these algorithms is to construct a unitary operation in a higher-dimensional Hilbert space, which simulates the desired non-unitary evolution in a lower-dimensional Hilbert space. The Stinespring dilation algorithm requires a larger Hilbert space dimension, which makes it computationally and experimentally expensive, as compared to the Sz.-Nagy algorithm. The Sz.-Nagy algorithm has been used to experimentally simulate the single-qubit amplitude damping channel on the IBM quantum processor [23].

In this work, we experimentally implemented the Sz.-Nagy quantum algorithm to simulate open quantum dynamics on an ensemble NMR quantum information processor. In order to simulate the given quantum dynamics of an open quantum system, the Sz.-Nagy algorithm requires prior knowledge of the corresponding complete set of Kraus operators. However, in a realistic scenario, the Kraus operators might not directly available. In such

^{*} ph16010@iisermohali.ac.in

[†] arvind@iisermohali.ac.in

[‡] kavita@iisermohali.ac.in

cases, one has to first compute the complete set of Kraus operators before proceeding with the implementation of the Sz.-Nagy algorithm. We used process tomography to first compute the process matrix which characterizes the given quantum process [24]. Using unitary diagonalization, we then compute the complete set of Kraus operators corresponding to a general quantum channel, using Lindblad generators. To demonstrate the efficacy of the Sz.-Nagy algorithm, we experimentally simulated two non-unitary quantum processes acting on a two-qubit system: a phase damping channel acting independently on the two qubits where the Kraus operators are already known, and a magnetic field gradient pulse (MFGP), where the Kraus operators are not directly available and need to be computed. Further, to validate the quality of the experimentally simulated quantum channel, we perform convex optimization-based full quantum process tomography [25, 26].

This paper is organized as follows: The details of the Sz.-Nagy dilation algorithm are given in Section II. The details of using the Sz.-Nagy algorithm to simulate two-qubit non-unitary quantum processes are given in Section III, with the experimental parameters detailed in Section III A. The experimental implementations of the Sz.-Nagy algorithm to simulate an independent phase damping channel and to simulate an MFGP acting on two NMR qubits are described in Section III B and III C, respectively. Section IV contains a few concluding remarks.

II. TIME EVOLUTION OF OPEN QUANTUM SYSTEMS AND THE SZ.-NAGY ALGORITHM

The Sz.-Nagy algorithm allows the density matrix of the system to evolve from its initial density matrix ρ to a density matrix $\rho(t)$ at time t , under a given evolution model. To mathematically represent the framework of the Sz.-Nagy algorithm, consider the operator-sum representation form for the time evolution of the density matrix (also called the Kraus operator representation) [27]:

$$\rho(t) = \sum_i A_i \rho A_i^\dagger \quad (1)$$

where the A_i s are Kraus operators satisfying $\sum_i A_i^\dagger A_i = I$. In order to implement the Sz.-Nagy algorithm to simulate any given open quantum dynamics, one requires the complete set of corresponding Kraus operators given in Eq.1.

The Sz.-Nagy algorithm states that, for any contraction operator W acting on a vector v in a Hilbert space \mathcal{H}_1 , one can construct a corresponding unitary dilation unitary operator U_w in a larger Hilbert space \mathcal{H}_2 , such that [23]:

$$W^m = P_{\mathcal{H}_1} U_w^m P_{\mathcal{H}_1}, \quad m \leq N \quad (2)$$

where $P_{\mathcal{H}_1}$ is the projection operator which projects the output vector into the space \mathcal{H}_1 , $\dim(\mathcal{H}_2) > \dim(\mathcal{H}_1)$, and

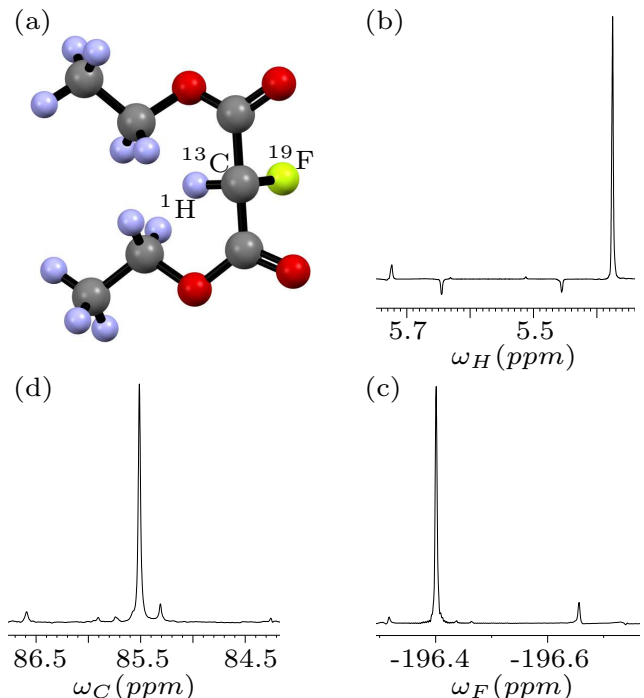


FIG. 1. (a) Molecular structure of ^{13}C -labeled diethyl fluoromalonate used as the three-qubit quantum system. The spectra shown in (b), (c) and (d) correspond to the ^1H , ^{19}F and ^{13}C spins respectively, obtained after applying a 90° read-out pulse on the $|000\rangle$ pseudopure state. The J -couplings between different nuclei are: $J_{HF} = 47.5$ Hz, $J_{HC} = 161.5$ Hz and $J_{FC} = -191.7$ Hz. The spin-lattice relaxation times measured for different nuclei are: $T_1^H = 3.0 \pm 0.34$ s, $T_1^F = 3.3 \pm 0.15$ s and $T_1^C = 3.2 \pm 0.38$ s, while the spin-spin relaxation times measured for different nuclei are: $T_2^H = 1.3 \pm 0.24$ s, $T_2^F = 1.4 \pm 0.22$ s and $T_2^C = 1.2 \pm 0.18$ s.

m and N are integers. Note that the operator W is said to be a ‘contraction’ if it preserves or shrinks the norm of any vector i.e. $\|W\| = \sup \frac{\|Wv\|}{\|v\|} \leq 1$. Eq.2 implies that the action of the contraction W , applied up to N times in space \mathcal{H}_1 can be simulated via the corresponding unitary dilation U_w applied up to N times on space \mathcal{H}_2 , given that the input vector lies in \mathcal{H}_1 and the output vector is projected into \mathcal{H}_1 .

Consider the set of Kraus operators $\{A_i\}$ (Eq. 1), corresponding to a given quantum process, which evolve the initial density matrix to $\rho(t)$. The Kraus operator A has to be a ‘contraction operator’, in order to find its corresponding unitary dilation operator. For a general proof that any Kraus operator satisfies all properties to be a ‘contraction operator’ see Reference [23]). For simplicity, consider an n -qubit system with a corresponding Hilbert space \mathcal{H} of dimension 2^n , and let the initial density matrix ρ be in a pure state i.e. $\rho = |\phi\rangle\langle\phi|$. In this case, the steps to implement the Sz.-Nagy algorithm to simulate Eq.1, are as follows [23]:

1. Prepare the pure input state $|\Phi\rangle = |0\rangle \otimes |\phi\rangle$ in a larger Hilbert space of dimension 2^{n+1} with the

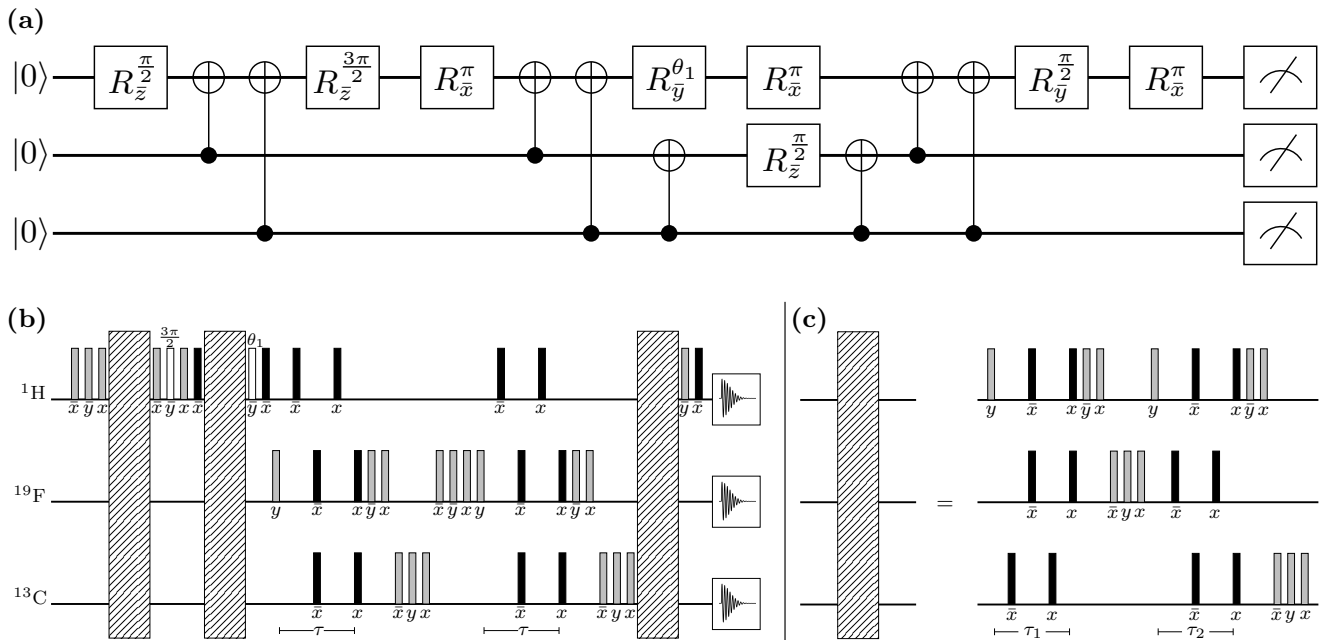


FIG. 2. (a) Quantum circuit to simulate the action of the Kraus operator A_1 of the phase damping channel on the initial state $|00\rangle$ using the Sz.-Nagy algorithm. The unitary dilation operator U_{A_1} is realized using eight CNOT gates and eight single-qubit rotation gates R_ϕ^θ . (b) NMR implementation of the quantum circuit given in (a). Gray and black filled rectangles represent $\pi/2$ and π pulses, respectively. The angles of the pulses represented by unfilled rectangles are shown above each pulse, where $\theta_1 = 0.3737 * \frac{\pi}{2}$. The dashed rectangular blocks consist of a set of pulses which have been expanded and represented in panel (c). The phases are written below the corresponding pulse. The free evolution time periods are set to $\tau = 0.0078$ s, $\tau_1 = 0.0105$ s and $\tau_2 = 0.0031$ s, respectively. The measurement box is indicated by a decaying time-domain NMR signal.

help of one ancillary qubit.

2. Apply the unitary operation U_{A_i} operation on the input state $|\Phi\rangle$, where U_{A_i} is the minimal unitary dilation of A_i (with $N = 1$) given by:

$$U_{A_i} = \begin{pmatrix} A_i & D_{A_i}^\dagger \\ D_{A_i} & -A_i^\dagger \end{pmatrix} \quad (3)$$

where $D_{A_i} = \sqrt{I - A_i^\dagger A_i}$ [23].

3. Project the output vector $U_{A_i}|\Phi\rangle$ into a smaller Hilbert space \mathcal{H} , using the appropriate projection operator $P_{\mathcal{H}}$, the dimension of \mathcal{H} being 2^n .
4. Repeat the above steps for the remaining Kraus operators, and sum over all output density matrices obtained after Step 3, in order to compute the effect of the given quantum process on the input state ρ .

Note that if the initial density matrix is in a mixed state i.e. $\rho = \sum_j p_j |\phi_j\rangle\langle\phi_j|$, then one has to repeat the Sz.-Nagy algorithm for all $|\phi_j\rangle$, in order to obtain the effect of a given quantum process on the initial mixed-state density matrix.

III. EXPERIMENTALLY SIMULATING TWO-QUBIT NON-UNITARY QUANTUM PROCESSES

We now proceed towards experimentally implementing the Sz.-Nagy algorithm in order to simulate a two-qubit pure phase damping channel and an MFGP process on an NMR quantum information processor, with the help of one ancillary qubit.

A. Experimental details

We used ^{13}C -labeled diethyl fluoromalonate dissolved in an acetone- D_6 as the three-qubit system, and assigned the ^1H , ^{19}F and ^{13}C spins as the first, second and third qubit, respectively (see Fig. 1 for experimental parameters). The Hamiltonian for a system of three spin-1/2 nuclei in the rotating frame is given by:

$$H = - \sum_{i=1}^3 \omega_i I_{iz} + \sum_{i,j=1, i>j}^3 J_{ij} I_{iz} I_{jz} \quad (4)$$

where ω_i is the chemical shift of the i th spin, J_{ij} is the scalar coupling strength between the i th and j th spins and I_{iz} represents the z -component of the spin angular momentum of the i th nucleus. State initialization was

achieved by preparing a pseudopure state (PPS) corresponding to $|000\rangle$ from the thermal state the using spatial averaging technique [28]. The density matrix ρ_{000} corresponding to $|000\rangle$ PPS is given by:

$$\rho_{000} = \left(\frac{1-\epsilon}{8}\right)I_8 + \epsilon|000\rangle\langle 000| \quad (5)$$

where $\epsilon \approx 10^{-5}$ denotes the bulk magnetization of the spin ensemble at room temperature and I_8 is the 8×8 identity matrix.

We performed convex optimization based quantum process tomography to reconstruct the experimental process matrix that characterizes the given quantum process. The process and state fidelity is calculated using the measure $\mathcal{F}(\chi_{\text{expt}}, \chi_{\text{theo}})$ [29]:

$$\mathcal{F}(\chi_{\text{expt}}, \chi_{\text{theo}}) = \frac{|\text{Tr}[\chi_{\text{expt}}\chi_{\text{theo}}^\dagger]|}{\sqrt{\text{Tr}[\chi_{\text{expt}}^\dagger\chi_{\text{expt}}]\text{Tr}[\chi_{\text{theo}}^\dagger\chi_{\text{theo}}]}} \quad (6)$$

where χ_{expt} (ρ_{expt}) and χ_{theo} (ρ_{theo}) define the experimental and theoretical process (density) matrices, respectively.

B. Simulating a two-qubit phase damping channel

The phase damping channel is well known and plays an important role in solution NMR, where it is responsible for the transverse relaxation of the spin ensemble. In some real-life situations, the low experimental fidelity of certain quantum gates (with long implementation times) can be ascribed to the deleterious effects of the phase damping channel. Several studies have focused on protecting fragile quantum coherences in the presence of phase damping[30–33].

We use the superoperator form to describe the open quantum dynamics of a system evolving under the action of a phase damping channel, where the generator of the phase damping process is available [34]. Let \mathcal{Z}_1 and \mathcal{Z}_2 denote the generators corresponding to the phase damping channel acting independently on qubit 1 and qubit 2, respectively. The matrix form of the generators \mathcal{Z}_1 and \mathcal{Z}_2 is given by [33, 34]:

$$\begin{aligned} \mathcal{Z}_1 &= \text{diag}[0, 0, -\gamma_1, -\gamma_1, 0, 0, -\gamma_1, -\gamma_1, -\gamma_1, -\gamma_1, 0, 0, \\ &\quad -\gamma_1, -\gamma_1, 0, 0] \\ \mathcal{Z}_2 &= \text{diag}[0, -\gamma_2, 0, -\gamma_2, -\gamma_2, 0 - \gamma_2, 0, 0, -\gamma_2, 0 - \gamma_2, \\ &\quad -\gamma_2, 0, -\gamma_2, 0] \end{aligned}$$

where γ_1 and γ_2 are the phase damping rates for qubit 1 and qubit 2, respectively. The resultant process is denoted by the superoperator Ξ which consists of the simultaneous action of phase damping channel independently acting on qubit 1 and qubit 2 and has the generator $\mathcal{Z} = \mathcal{Z}_1 + \mathcal{Z}_2$. The time evolution of the initial two-qubit density matrix ρ can be written as [34]:

$$\rho(t) = \Xi(\rho) = e^{\mathcal{Z}t}(\bar{\rho}) \quad (7)$$

In order to simulate Eq. 7 using the Sz.-Nagy algorithm, one requires the complete set of Kraus operators corresponding to the phase damping process. We used the standard quantum process tomography (QPT) technique to compute Kraus operators as follows:

1. Construct the complete set of linearly independent initial input density matrices.
2. Estimate output density matrices by evolving each input density matrix using Eq. 7.
3. From knowledge of the input and output density matrices, compute the process matrix χ using the standard QPT protocol.
4. Using unitary diagonalization of χ matrix as [29]: $\chi = VDV^\dagger$, compute the complete set of Kraus operators as:

$$A_i = \sqrt{d_i} \sum_j V_{ji} E_j \quad (8)$$

where A_i s are the Kraus operators, d_i s are diagonal elements of the matrix D , V_{ji} s are elements of the matrix V and the E_j s form a fixed operator basis. The diagonal elements of matrix D are eigenvalues of the χ matrix and the columns of matrix V are the corresponding normalized eigenvectors of the χ matrix.

Note that the Kraus operators corresponding to the two-qubit phase damping channel are already known in literature and one could have directly use them here. However we have used the superoperator form given in Eq. (7), in order to illustrate our method which is general and can be used to describe quantum processes where the Kraus operators are not directly available (such as correlated phase damping channels [34]). The unitary dilation operators $\{U_{A_i}\}$ corresponding to each Kraus operator $\{A_i\}$ were computed using Eq. 3. We set the values of the phase damping rates to be $\gamma_1 = 1.4$ and $\gamma_2 = 1.5$, and evolved the initial density matrix for a time $t = 2$ s using Eq. 7. We note here that the time required to implement a unitary dilation operator on two NMR qubits depends crucially on the implementation times of the CNOT gates, which for our system turns out to be in the range of 3-11 ms. The total time required to implement all the four unitary dilation operators required to simulate the phase damping channel is hence ≈ 80 ms. The spin-spin relaxation times (T_2) of the three NMR qubits (which characterizes the natural phase damping channel active in the NMR system) are: $T_2^H = 1.3$ s, $T_2^F = 1.4$ s, $T_2^C = 1.2$ s, respectively. Since the time required to implement the unitary dilation operators is much smaller than the natural phase damping rates of the system, the experimental implementation of the simulated phase damping channel is largely unaffected by the natural NMR noise.

The complete set of Kraus operators which evolve the initial density matrix under the action of independent

phase damping channels on each qubit, for given values of γ_1 , γ_2 and t , is given in Appendix A. It turns out that there are four non-zero Kraus operators which characterize the phase damping channel for the given parameter values.

Fig. 2 demonstrates the implementation of the Sz.-Nagy algorithm to simulate the action of Kraus operator A_1 (see Appendix A) on the two-qubit initial input state $|\phi\rangle\langle\phi| = |00\rangle\langle 00|$. The initial two-qubit state $|00\rangle$ is encoded in a three-qubit input state as $|000\rangle = |0\rangle_a \otimes |00\rangle_{\text{main}}$. The quantum circuit given in Fig.2 (a) represents the action of the unitary dilation operator U_{A_1} on the input state ρ_{000} , followed by measurement. We used the column-by-column decomposition (COC) method [35, 36] to decompose three-qubit unitary dilation operators $\{U_{A_i}\}$. Using the COC method, U_{A_1} is realized using eight CNOT gates and eight single-qubit rotation gates R_ϕ^θ (where ϕ denotes the axis of rotation and θ denotes the angle of rotation). The COC decompositions of the other unitary dilation operators are given in Appendix A. We note here in passing that the same quantum circuit one can also be used to simulate the action of A_1 on arbitrary initial two-qubit states $\rho = |\phi\rangle\langle\phi|$, in which case we merely need to prepare the three-qubit system in the state $|0\rangle \otimes |\phi\rangle$. Further, the arbitrary initial input state $|\phi\rangle$ of the two-qubit system lies in the smaller Hilbert space which is spanned by the vectors: $|000\rangle$, $|001\rangle$, $|010\rangle$ and $|011\rangle$. The action of projecting the higher-dimensional output state into this smaller Hilbert space is equivalent to estimating a 4×4 dimensional partial density matrix (corresponding to the first four rows and columns of the higher-dimensional output density matrix). The NMR pulse sequence to implement the quantum circuit is depicted in Fig.2(b). Spin-selective high-power rf pulses were used to implement single-qubit rotation gates. Filled gray and black rectangles in Fig. 2(b) represent $\pi/2$ and π pulses respectively, while unfilled rectangles represent pulses with their corresponding flip angles given above each pulse; the value of θ_1 was set to $0.3737 * \frac{\pi}{2}$. The three dashed boxes consist of a set of pulses which have been expanded and depicted in Fig. 2(c). The phase of each pulse is shown below every rectangle. The various free evolution time periods were set to $\tau = 0.0078$ s, $\tau_1 = 0.0105$ s and $\tau_2 = 0.0031$ s, respectively. The measurement box depict the decaying time domain NMR signal (the free induction decay (FID)) which is Fourier transformed to obtain the NMR spectrum. Finally, tomographic measurements were performed to compute density matrix elements $\{\rho_{ij}, 0 \leq i, j \leq 4\}$. The normalized trace distance between the experimentally obtained output Hermitian matrix $(A_1\rho_{00}A_1^\dagger)_{\text{exp}}$ and the theoretically expected matrix $(A_1\rho_{00}A_1^\dagger)_{\text{the}}$ turns out to be 0.9885. A similar quantum circuit and NMR pulse sequence is employed to simulate the MFGP, where the action of the Kraus operator A_1 (Appendix B) on the state $|00\rangle$ can be simulated using the unitary dilation operator U (Eq. B1 in Appendix B), via the COC method and 9 CNOT gates and 18 local

rotations.

TABLE I. The normalized trace distance between the experimentally obtained output Hermitian matrix $(A_i\rho_jA_i^\dagger)_{\text{exp}}$ and the theoretically expected matrix $(A_i\rho_jA_i^\dagger)_{\text{the}}$ for the phase damping channel.

	A_1	A_2	A_3	A_4
$ 00\rangle$	0.9885	0.9881	0.9911	0.9773
$ 01\rangle$	0.9769	0.9909	0.9901	0.9804
$ 0+\rangle$	0.9105	0.9825	0.9877	0.9788
$ 0-\rangle$	0.8984	0.9905	0.9585	0.9613
$ 10\rangle$	0.9625	0.9579	0.9873	0.9780
$ 11\rangle$	0.9071	0.9519	0.9847	0.9747
$ 1+\rangle$	0.8193	0.9447	0.9538	0.9823
$ 1-\rangle$	0.7236	0.9212	0.9286	0.9494
$ +0\rangle$	0.9625	0.9888	0.9251	0.9608
$ +1\rangle$	0.8733	0.9447	0.9892	0.9856
$ ++\rangle$	0.8697	0.9590	0.9712	0.9814
$ +-\rangle$	0.8974	0.9489	0.9506	0.9669
$ -0\rangle$	0.9149	0.9892	0.9205	0.9630
$ -1\rangle$	0.8168	0.9222	0.9946	0.9781
$ -+\rangle$	0.8105	0.9363	0.9819	0.9643
$ --\rangle$	0.8233	0.9518	0.9608	0.9594

For the phase damping channel, the normalized trace distance between the experimentally obtained output Hermitian matrix $(A_i\rho_jA_i^\dagger)$ and the theoretically expected matrix is given in Table I. High values of the normalized trace distance in Table I clearly demonstrates the successful experimental simulation of the action of a given Kraus operator on a given initial state. However, for all the initial quantum states, the values given in the first column corresponding to A_1 are relatively smaller than the values given in the other columns corresponding to A_2 , A_3 and A_4 , respectively. This is due to the fact that the experimental complexity involved in implementing U_{A_1} is relatively larger than U_{A_2} , U_{A_3} and U_{A_4} in terms of the number of CNOT gates which introduces more experimental errors in the implementation of U_{A_1} . In addition, it turns out that for some quantum states such as $|1+\rangle$, $|1-\rangle$, $|-1\rangle$, $|-+\rangle$ and $|--\rangle$ the values of trace distance are relatively small as compared to other states, which can be attributed to errors in initial state preparation.

Note that in order to obtain the final density matrix $\rho(t)$ evolved under a desired quantum channel one has to assemble all results from each Kraus operator. For the phase damping channel it turns out that four quantum circuits corresponding to each U_{A_i} need to be implemented to obtain the final $\rho(t)$. For completeness, we experimentally simulated the action of all Kraus operators corresponding to the phase damping channel on 16 linearly independent two-qubit density matrices. For all 16 states, the fidelities between the experimentally sim-

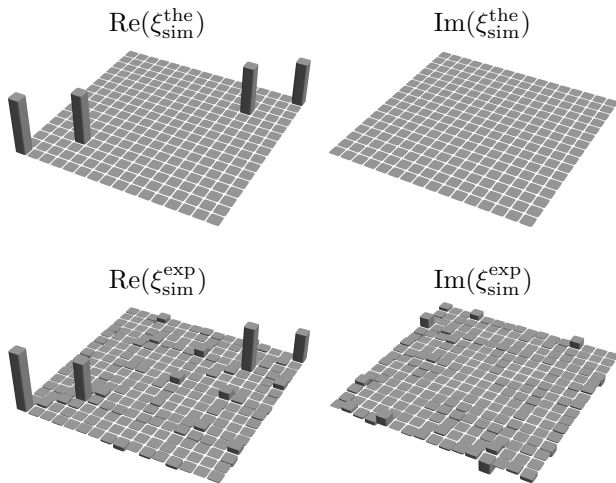


FIG. 3. Process matrices obtained by theoretically and experimentally simulating phase damping channels acting independently on each qubit in a two-qubit NMR system. The bar plots in the first column represent the real part of the process matrices of the theoretically simulated ($\text{Re}(\chi_{\text{theo}})$), and the experimentally obtained phase damping channel computed using convex optimization-based QPT ($\text{Re}(\chi_{\text{expt}})$), respectively. The bar plots in the second column represent the imaginary part of the respective process matrices.

ulated state using the Sz.-Nagy algorithm and the theoretically simulated state for the phase damping channel are given in Table II.

TABLE II. Fidelity between the experimentally and theoretically simulated two-qubit states evolving under independent phase damping channels.

State	Fidelity	State	Fidelity
$ 00\rangle$	0.9936	$ +0\rangle$	0.9568
$ 01\rangle$	0.9950	$ +1\rangle$	0.9564
$ 0+\rangle$	0.9734	$ ++\rangle$	0.9673
$ 0-\rangle$	0.9696	$ +-\rangle$	0.9607
$ 10\rangle$	0.9885	$ -0\rangle$	0.9444
$ 11\rangle$	0.9821	$ -1\rangle$	0.9343
$ 1+\rangle$	0.9521	$ -+\rangle$	0.9412
$ 1-\rangle$	0.9409	$ --\rangle$	0.9373

The high values of the fidelities given in Table II demonstrate the successful experimental simulation of the action of the phase damping channel on a given initial quantum state. Since the given set of 16 states forms a complete basis set, one can simulate the action of the phase damping channel on an arbitrary quantum state with fidelities ranging between 0.9343 and 0.9950.

C. Simulating a magnetic field gradient pulse

MFGP are extensively used in NMR and magnetic resonance imaging experiments, covering a wide range of applications, such as studies of molecular diffusion and spatial encoding for imaging [37–39]. Recently, a time and space discretization method was proposed to simulate shaped gradient pulses [40]. The action of a MFGP is similar to the phase damping channel, as it effectively kills the off-diagonal elements (coherences) of the density matrix in a controlled manner. In this study we employ the Sz.-Nagy algorithm to simulate two-qubit dynamics under the action of a shaped MFGP applied for a given duration.

A shaped MFGP has a strength that varies during its execution. The gradient pulse is defined by a list of values, with each element in the list defining the relative gradient strength during a particular time interval. The interval length is defined by the length of the entire gradient shape divided by the number of intervals. The gradient strength is expressed as a percentage of the maximum strength. In the NMR hardware, MFGP is applied using gradient coils. The parameters of the shaped gradient pulse used are: Sine shaped, duration $1000\mu\text{s}$, number of time intervals = 100, and an applied gradient strength of 15%.

In order to simulate the desired MFGP using the Sz.-Nagy algorithm, we first need to characterize it and then compute the corresponding Kraus operators. We used convex optimization based quantum process tomography to experimentally characterize the desired MFGP and then computed the complete set of Kraus operator using Eq. (8). To achieve this, we experimentally prepared the complete set of linearly independent initial two-qubit quantum states: $\{|0\rangle, |1\rangle, |+\rangle, |-\rangle\}^{\otimes 2}$ where $|+\rangle = (|0\rangle + |1\rangle)/\sqrt{2}$ and $|-\rangle = (|0\rangle + i|1\rangle)/\sqrt{2}$. The desired MFGP is then applied on the initial input states using gradient coils. By performing full quantum state tomography of all output states we compute the process matrix χ characterizing the MFGP and the complete set of Kraus operators are calculated using Eq. (8). The Sz.-Nagy algorithm is finally employed to simulate the MFGP using only unitary operations. At the end, the process fidelity is computed between the experimental process matrix characterizing the MFGP and the experimental process matrix of the simulated MFGP. The complete set of Kraus operators and corresponding unitary dilation operators for the shaped MFGP are given in Appendix B.

For the shaped MFGP operation, the normalized trace distance between the simulated output hermitian matrix $(A_i \rho_j A_i^\dagger)_{\text{sim}}^{\text{exp}}$ using the Sz.-Nagy algorithm and the experimentally obtained matrix $(A_i \rho_j A_i^\dagger)_{\text{qpt}}^{\text{exp}}$ via quantum process tomography is given in Table III. For the case of the MFGP process, the Kraus operators which are to be experimentally simulated are themselves computed from experimentally constructed process matrix and also have

TABLE III. The normalized trace distance between experimentally simulated output hermitian matrix $(A_i \rho_j A_i^\dagger)_{\text{sim}}^{\text{exp}}$ using SND algorithm and experimentally obtained matrix $(A_i \rho_j A_i^\dagger)_{\text{qpt}}^{\text{exp}}$ via quantum process tomography of MFGP implemented on two qubits.

	A_1	A_2	A_3	A_4
$ 00\rangle$	0.8671	0.9541	0.9704	0.9182
$ 01\rangle$	0.8919	0.9866	0.9602	0.9884
$ 0+\rangle$	0.8705	0.8359	0.9164	0.9476
$ 0-\rangle$	0.9204	0.8132	0.9208	0.8494
$ 10\rangle$	0.9925	0.8317	0.9225	0.9685
$ 11\rangle$	0.9732	0.9627	0.9805	0.9345
$ 1+\rangle$	0.9573	0.7373	0.9715	0.7062
$ 1-\rangle$	0.9025	0.8016	0.9654	0.6549
$ +0\rangle$	0.7818	0.6658	0.9220	0.9097
$ +1\rangle$	0.8430	0.9697	0.8851	0.6822
$ ++\rangle$	0.7669	0.7404	0.8063	0.7433
$ +-\rangle$	0.8397	0.7700	0.7414	0.6495
$ -0\rangle$	0.7312	0.7444	0.9365	0.9148
$ -1\rangle$	0.8902	0.9767	0.8799	0.6585
$ -+\rangle$	0.8247	0.8123	0.8282	0.7211
$ --\rangle$	0.8410	0.8181	0.8395	0.6690

TABLE IV. Fidelity between experimentally simulated and experimentally implemented two-qubit state under the action of a magnetic field gradient pulse.

State	Fidelity	State	Fidelity
$ 00\rangle$	0.9818	$ +0\rangle$	0.9069
$ 01\rangle$	0.9884	$ +1\rangle$	0.9440
$ 0+\rangle$	0.9893	$ ++\rangle$	0.9096
$ 0-\rangle$	0.9619	$ +-\rangle$	0.8888
$ 10\rangle$	0.9719	$ -0\rangle$	0.8946
$ 11\rangle$	0.9754	$ -1\rangle$	0.9514
$ 1+\rangle$	0.9577	$ -+\rangle$	0.9311
$ 1-\rangle$	0.9426	$ --\rangle$	0.9097

a relatively high experimental complexity in terms of the number of CNOT gates required to experimentally implement the unitary dilation operators. This could be a possible explanation for the smaller values of the trace distance in Table III for the MFGP process, as compared to the phase damping channel.

For the MFGP operation, four quantum circuits corresponding to each U_{A_i} need to be implemented to obtain the final $\rho(t)$. For completeness, we experimentally simulated the action of all Kraus operators on 16 linearly independent two-qubit density matrices for the MFGP process. For all 16 states, the fidelities between the experimentally simulated state using the Sz.-Nagy algorithm and the theoretically simulated state corresponding to

the MFGP operation are given in Table IV. Since the the set of 16 states given in Table IV forms a complete basis set, the action of the MFGP can be simulated on any arbitrary quantum state with fidelities ranging between 0.8888 and 0.9893.

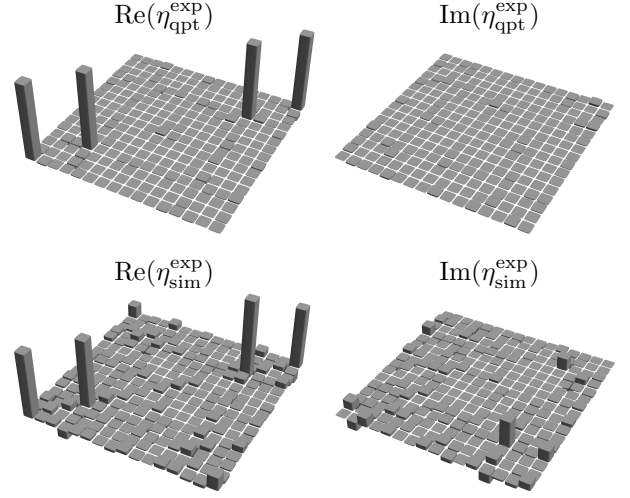


FIG. 4. In the top panel, $\text{Re}(\eta_{\text{qpt}}^{\text{exp}})$ and $\text{Im}(\eta_{\text{qpt}}^{\text{exp}})$ denote the real and imaginary parts of the experimental process matrix obtained by performing quantum process tomography of the shaped MFGP applied on two qubits. In the bottom panel, $\text{Re}(\eta_{\text{sim}}^{\text{exp}})$ and $\text{Im}(\eta_{\text{sim}}^{\text{exp}})$ represent the real and imaginary parts of the process matrix of the same MFGP experimentally simulated using the Sz.-Nagy algorithm. The process fidelity between $\eta_{\text{qpt}}^{\text{exp}}$ and $\eta_{\text{sim}}^{\text{exp}}$ turns out to be 0.8824.

For the phase damping channel, the process fidelity is computed between $(\xi_{\text{sim}}^{\text{exp}})$ obtained via the experimentally simulated channel and $(\xi_{\text{sim}}^{\text{the}})$ obtained via the theoretically simulated channel. For the shaped MFGP process, the process fidelity is computed between $(\eta_{\text{qpt}}^{\text{exp}})$ obtained via the experimentally simulated shaped MFGP and $(\eta_{\text{qpt}}^{\text{exp}})$ obtained via quantum process tomography performed on experimentally implemented shaped MFGP. For the phase damping channel, the computed process fidelity turns out to be 0.9148 and the respective tomographs are compared in Fig. 3, while for the shaped MFGP process, the computed process fidelity turns out to be 0.8824 and the respective tomographs are compared in Fig. 4, where the tomographs are plotted on the same scale. For both the phase damping channel and the MFGP process, the real part of the process matrix has only four non-zero elements corresponding to $E_1 = I \otimes I$, $E_4 = I \otimes \sigma_z$, $E_{13} = \sigma_z \otimes I$, and $E_{16} = \sigma_z \otimes \sigma_z$, which are the set of Kraus operators [5]. The imaginary part of the process matrix for both processes turns out to be almost zero. From Figs.3 and 4 it can be seen that the action of the shaped MFGP and the phase damping channel is similar, in effectively destroying the off-diagonal elements of the density matrix. The deviations in the simulated process matrix from the desired process matrix arises due to experimental errors in state preparation, implementa-

tion of unitary dilation operators and inevitable systematic errors. These errors can be reduced using appropriate optimization protocols [41]. Particularly for the MFGP process, the experimental implementation of all four unitary dilation operators requires 9 CNOT gates (*i.e.* 9 CNOT gates \times 4 Kraus operators = 36 CNOT gates in total to simulate the MFGP process), while for the phase damping channel, the experimental implementation of the unitary dilation operator U_{A_1} , U_{A_2} , U_{A_3} and U_{A_4} requires 8, 3, 3 and 0 CNOT gates, respectively (*i.e.* 14 CNOT gates in total to simulate the phase damping channel). Hence the experimental errors are higher in simulating the MFGP process as compared to the phase damping channel, which is reflected in lower values of the process fidelities in Tables III and IV.

IV. CONCLUSIONS

We experimentally implemented the Sz.-Nagy algorithm to simulate an independent phase damping channel and a shaped MFGP acting on two qubits, with the help of one ancilla qubit on an NMR quantum information processor. We designed a protocol to compute the complete set of Kraus operators using quantum process tomography and the unitary diagonalization technique. To validate the quality of the experimentally simulated

quantum process, we performed quantum process tomography based on the constrained convex optimization technique. Our results demonstrate that the experimental implementation of the Sz.-Nagy algorithm is viable, since it requires only one ancilla qubit to simulate arbitrary-dimensional open quantum dynamics. The protocol is general and valid for arbitrary quantum processes and can be adapted for other physical platforms to simulate complex quantum processes using the Sz.-Nagy algorithm. However, implementing the unitary dilation operator corresponding to a given Kraus operator remains a challenging task. The need of the hour is hence to develop computationally efficient algorithms to decompose a given unitary dilation operator into a universal set of quantum gates.

ACKNOWLEDGMENTS

All the experiments were performed on a Bruker Avance-III 600 MHz FT-NMR spectrometer at the NMR Research Facility of IISER Mohali. Arvind acknowledges financial support from DST/ICPS/QuST/Theme-1/2019/General Project number Q-68. K.D. acknowledges financial support from DST/ICPS/QuST/Theme-2/2019/General Project number Q-74.

-
- [1] R. P. Feynman, *Int. J. Theor. Phys.* **21**, 467 (1982).
 - [2] S. Lloyd, *Science* **273**, 1073 (1996).
 - [3] I. Kassal, J. D. Whitfield, A. Perdomo-Ortiz, M.-H. Yung, and A. Aspuru-Guzik, *Annu. Rev. Phys. Chem.* **62**, 185 (2011), pMID: 21166541, <https://doi.org/10.1146/annurev-physchem-032210-103512>.
 - [4] I. M. Georgescu, S. Ashhab, and F. Nori, *Rev. Mod. Phys.* **86**, 153 (2014).
 - [5] M. A. Nielsen and I. L. Chuang, *Quantum Computation and Quantum Information* (Cambridge University Press, Cambridge UK, 2010).
 - [6] D. P. DiVincenzo, *Fortschritte der Physik* **48**, 771 (2000).
 - [7] R. Harper, S. T. Flammia, and J. J. Wallman, *Nat. Phys.* **16**, 1184 (2020).
 - [8] H.-P. Breuer and F. Petruccione, *The Theory of Open Quantum Systems* (Oxford University Press, Oxford, 2007) p. 656.
 - [9] I. Rotter and J. P. Bird, *Rep. Prog. Phys.* **78**, 114001 (2015).
 - [10] N. Zuniga-Hansen, Y.-C. Chi, and M. S. Byrd, *Phys. Rev. A* **86**, 042335 (2012).
 - [11] S.-J. Wei, D. Ruan, and G.-L. Long, *Sci. Rep.* **6**, 30727 (2016).
 - [12] C. Zheng, *Sci. Rep.* **11**, 3960 (2021).
 - [13] R. Di Candia, J. S. Pedernales, A. del Campo, E. Solano, and J. Casanova, *Sci. Rep.* **5**, 9981 (2015).
 - [14] N.-N. Zhang, M.-J. Tao, W.-T. He, X.-Y. Chen, X.-Y. Kong, F.-G. Deng, N. Lambert, and Q. Ai, *Front. Phys.* **16**, 51501 (2021).
 - [15] B.-H. Liu, L. Li, Y.-F. Huang, C.-F. Li, G.-C. Guo, E.-M. Laine, H.-P. Breuer, and J. Piilo, *Nat. Phys.* **7**, 931 (2011).
 - [16] N. K. Bernardes, J. P. S. Peterson, R. S. Sarthour, A. M. Souza, C. H. Monken, I. Roditi, I. S. Oliveira, and M. F. Santos, *Sci. Rep.* **6**, 33945 (2016).
 - [17] Z.-D. Liu, H. Lyyra, Y.-N. Sun, B.-H. Liu, C.-F. Li, G.-C. Guo, S. Maniscalco, and J. Piilo, *Nat. Commun.* **9**, 3453 (2018).
 - [18] S. Patsch, S. Maniscalco, and C. P. Koch, *Phys. Rev. Research* **2**, 023133 (2020).
 - [19] G. García-Pérez, M. A. C. Rossi, and S. Maniscalco, *npj Quantum Inf.* **6**, 1 (2020).
 - [20] S. Dogra, A. A. Melnikov, and G. S. Paraoanu, *Commun. Phys.* **4**, 26 (2021).
 - [21] M. E. Shirokov, *J. Math. Phys.* **61**, 082204 (2020), <https://doi.org/10.1063/1.5134660>.
 - [22] K. Head-Marsden, S. Krastanov, D. A. Mazziotti, and P. Narang, *Phys. Rev. Research* **3**, 013182 (2021).
 - [23] Z. Hu, R. Xia, and S. Kais, *Sci. Rep.* **10**, 3301 (2020).
 - [24] A. Gaikwad, D. Rehal, A. Singh, Arvind, and K. Dorai, *Phys. Rev. A* **97**, 022311 (2018).
 - [25] A. Gaikwad, K. Shende, and K. Dorai, *International Journal of Quantum Information* **19**, 2040004 (2021), <https://doi.org/10.1142/S0219749920400043>.
 - [26] A. Gaikwad, Arvind, and K. Dorai, "Efficient experimental characterization of quantum processes via compressed sensing on an NMR quantum processor," (2021), arXiv:2109.13189 [quant-ph].

- [27] K. Kraus, A. Bohm, J. Dollard, and W. Wootters, *States, Effects, and Operations: Fundamental Notions of Quantum Theory* (Springer-Verlag Berlin Heidelberg, 1983).
- [28] I. S. Oliveira, T. J. Bonagamba, R. S. Sarthour, J. C. C. Freitas, and E. R. deAzevedo, *NMR Quantum Information Processing* (Elsevier, Linacre House, Jordan Hill, Oxford OX2 8DP, UK, 2007).
- [29] A. Gaikwad, Arvind, and K. Dorai, *Quant. Inf. Proc.* **20**, 19 (2021).
- [30] H. Singh, Arvind, and K. Dorai, *EPL (Europhysics Letters)* **118**, 50001 (2017).
- [31] H. Singh, Arvind, and K. Dorai, *Phys. Rev. A* **95**, 052337 (2017).
- [32] H. Singh, Arvind, and K. Dorai, *Phys. Rev. A* **97**, 022302 (2018).
- [33] H. Singh, Arvind, and K. Dorai, *Pramana* **94**, 160 (2020).
- [34] A. M. Childs, I. L. Chuang, and D. W. Leung, *Phys. Rev. A* **64**, 012314 (2001).
- [35] R. Iten, R. Colbeck, I. Kukuljan, J. Home, and M. Christandl, *Phys. Rev. A* **93**, 032318 (2016).
- [36] R. Iten, O. Reardon-Smith, E. Malvetti, L. Mondada, G. Pauvert, E. Redmond, R. S. Kohli, and R. Colbeck, "Introduction to universalqcompiler," (2021), arXiv:1904.01072 [quant-ph].
- [37] D. Le Bihan and H. Johansen-Berg, *NeuroImage* **61**, 324 (2012).
- [38] G. Pagés, V. Gilard, R. Martino, and M. Malet-Martino, *Analyst* **142**, 3771 (2017).
- [39] K. S. Han, J. D. Bazak, Y. Chen, T. R. Graham, N. M. Washton, J. Z. Hu, V. Murugesan, and K. T. Mueller, *Chem. Mater.* **33**, 8562 (2021), <https://doi.org/10.1021/acs.chemmater.1c02891>.
- [40] J. P. S. Peterson, H. Katiyar, and R. Laflamme, "Fast simulation of magnetic field gradients for optimization of pulse sequences," (2020), arXiv:2006.10133 [quant-ph].
- [41] A. Devra, P. Prabhu, H. Singh, Arvind, and K. Dorai, *Quant. Inf. Proc.* **17**, 67 (2018).

Appendix A: Kraus operators & unitary dilation operators for phase damping channel

The complete set of Kraus operators corresponding to an independent phase damping channel, acting on the two-qubit system with parameter values $\gamma_1 = 1.4$, $\gamma_2 = 1.5$ and $t = 2$ sec, is given below:

$$A_1 = \begin{pmatrix} -0.4723 + 0.i & 0. + 0.i & 0. + 0.i & 0. + 0.i \\ 0. + 0.i & 0.4723 + 0.i & 0. + 0.i & 0. + 0.i \\ 0. + 0.i & 0. + 0.i & 0.4723 + 0.i & 0. + 0.i \\ 0. + 0.i & 0. + 0.i & 0. + 0.i & -0.4723 + 0.i \end{pmatrix}$$

$$A_2 = \begin{pmatrix} 0.0181 - 0.4961i & 0. + 0.i & 0. + 0.i & 0. + 0.i \\ 0. + 0.i & 0.0181 - 0.4961i & 0. + 0.i & 0. + 0.i \\ 0. + 0.i & 0. + 0.i & -0.0181 + 0.4961i & 0. + 0.i \\ 0. + 0.i & 0. + 0.i & 0. + 0.i & -0.0181 + 0.4961i \end{pmatrix}$$

$$A_3 = \begin{pmatrix} -0.0085 - 0.5019i & 0. + 0.i & 0. + 0.i & 0. + 0.i \\ 0. + 0.i & 0.0085 + 0.5019i & 0. + 0.i & 0. + 0.i \\ 0. + 0.i & 0. + 0.i & -0.0085 - 0.5019i & 0. + 0.i \\ 0. + 0.i & 0. + 0.i & 0. + 0.i & 0.0085 + 0.5019i \end{pmatrix}$$

$$A_4 = \begin{pmatrix} -0.5276 - 0.007i & 0. + 0.i & 0. + 0.i & 0. + 0.i \\ 0. + 0.i & -0.5276 - 0.007i & 0. + 0.i & 0. + 0.i \\ 0. + 0.i & 0. + 0.i & -0.5276 - 0.007i & 0. + 0.i \\ 0. + 0.i & 0. + 0.i & 0. + 0.i & -0.5276 - 0.007i \end{pmatrix}$$

The decomposition of the unitary dilation operators U_{A_i} corresponding to the Kraus operators for the phase damping channel are given below. We have used the column-by-column decomposition method to decompose a given unitary into single-qubit rotation gates and two-qubit CNOT gates.

1. $U_{A_1}: {}^1R_{\bar{x}}^{\pi} \cdot {}^1R_{\bar{y}}^{\frac{\pi}{2}} \cdot U_{\text{CNN}} \cdot \text{CNOT}_{32} \cdot {}^2R_{\bar{z}}^{\frac{\pi}{2}} \cdot \text{CNOT}_{32} \cdot {}^1R_{\bar{x}}^{\pi} \cdot {}^1R_{\bar{y}}^{\theta_1} \cdot U_{\text{CNN}} \cdot {}^1R_{\bar{x}}^{\pi} \cdot {}^1R_{\bar{z}}^{\frac{3\pi}{2}} \cdot U_{\text{CNN}} \cdot {}^1R_{\bar{z}}^{\frac{\pi}{2}}$
where $U_{\text{CNN}} = \text{CNOT}_{31} \cdot \text{CNOT}_{21}$ and $\theta_1 = 0.5870$
2. $U_{A_2} = {}^1R_{\bar{x}}^{\pi} \cdot {}^1R_{\bar{y}}^{\frac{\pi}{2}} \cdot \text{CNOT}_{21} \cdot {}^1R_{\bar{x}}^{\theta_3} \cdot {}^1R_{\bar{y}}^{\theta_2} \cdot \text{CNOT}_{21} \cdot {}^1R_{\bar{x}}^{\theta_1} \cdot {}^1R_{\bar{z}}^{\frac{\pi}{2}} \cdot \text{CNOT}_{21} \cdot {}^2R_{\bar{z}}^{\frac{3\pi}{2}}$
where $\theta_1 = 3.0803$, $\theta_2 = 0.5329$, and $\theta_3 = 1.6059$

3. $U_{A_3} = {}^1R_{\bar{x}}^{\pi} \cdot {}^1R_{\bar{y}}^{\frac{\pi}{2}} \cdot \text{CNOT}_{31} \cdot {}^1R_{\bar{x}}^{\theta_3} \cdot {}^1R_{\bar{y}}^{\theta_2} \cdot \text{CNOT}_{31} \cdot {}^1R_{\bar{x}}^{\theta_1} \cdot {}^1R_{\bar{z}}^{\frac{\pi}{2}} \cdot \text{CNOT}_{31} \cdot {}^3R_{\bar{z}}^{\frac{3\pi}{2}}$
where $\theta_1 = 3.1711$, $\theta_2 = 0.5193$, and $\theta_3 = 1.5536$
4. $U_{A_4} = {}^1R_{\bar{z}}^{\theta_3} \cdot {}^1R_{\bar{y}}^{\theta_2} \cdot {}^1R_{\bar{z}}^{\theta_1}$ where $\theta_1 = 3.1549$, $\theta_2 = 2.0299$, and $\theta_3 = 0.0133$

where ${}^iR_{\phi}^{\theta}$ represents a single-qubit rotation gate acting on the i th qubit with the rotation angle θ and the rotation axis is denoted by ϕ and CNOT_{ij} represents a two-qubit CNOT gate with the i th qubit being the control and the j th qubit being the target qubit.

Appendix B: Kraus operators and unitary dilation operators for shaped MFGP

The complete set of Kraus operators corresponding to the desired shaped gradient pulse with parameter values given in Section III C applied on a two-qubit system were experimentally computed via the convex optimization based QPT method. The Kraus operators are given by:

$$\begin{aligned}
 A_1 &= \begin{pmatrix} 0.1231 - 0.0877i & -0.0038 + 0.0026i & -0.0077 + 0.0085i & 0.0023 + 0.0004i \\ 0.0122 - 0.0279i & -0.1899 - 0.1181i & 0.0101 + 0.0085i & 0.0097 + 0.006i \\ -0.0174 + 0.0165i & -0.0073 + 0.0042i & -0.3573 + 0.4876i & 0.0167 - 0.0073i \\ -0.0036 - 0.0034i & -0.0056 + 0.0133i & -0.0009 + 0.0275i & 0.5454 + 0.4572i \end{pmatrix} \\
 A_2 &= \begin{pmatrix} -0.0434 - 0.4568i & 0.0061 + 0.0085i & 0.0095 + 0.0121i & -0.0055 - 0.0064i \\ 0.0329 + 0.0096i & 0.181 - 0.4594i & -0.0029 + 0.0105i & -0.0003 + 0.0002i \\ 0.0017 - 0.0235i & 0.0036 - 0.003i & -0.35 - 0.3762i & 0.0141 - 0.0184i \\ -0.0055 - 0.0042i & 0.0124 - 0.007i & 0.012 + 0.0275i & 0.3231 - 0.3787i \end{pmatrix} \\
 A_3 &= \begin{pmatrix} -0.4842 - 0.5645i & 0.0305 + 0.0057i & 0.027 - 0.0027i & -0.0011 + 0.0033i \\ -0.0206 + 0.0166i & -0.327 + 0.0929i & 0.0007 - 0.0019i & 0.0034 - 0.0026i \\ 0.0102 + 0.0216i & -0.0024 + 0.0064i & 0.3035 - 0.2407i & 0.0096 + 0.0199i \\ -0.0005 - 0.0058i & 0.0024 + 0.0041i & 0.015 + 0.006i & -0.0094 + 0.4166i \end{pmatrix} \\
 A_4 &= \begin{pmatrix} 0.4475 + 0.0416i & -0.0139 + 0.0256i & -0.0099 + 0.0021i & 0.0055 + 0.0044i \\ -0.0239 - 0.0035i & -0.7081 + 0.2924i & -0.0143 - 0.0018i & 0.0063 - 0.0201i \\ 0.0027 - 0.0084i & 0.0055 + 0.0079i & -0.1662 - 0.4034i & 0.0107 - 0.0154i \\ 0.0045 - 0.0062i & 0.0167 - 0.0093i & -0.0253 + 0.0106i & 0.1022 - 0.1527i \end{pmatrix}
 \end{aligned}$$

The decomposition of unitary dilation operators U_{A_i} corresponding to respective Kraus operators are given below for a shaped gradient pulse. We used the column-by-column decomposition method to decompose a given unitary into single-qubit rotations and CNOT gates. It turns out that in the case of a shaped gradient pulse, the form of decomposition of unitary dilation operators corresponding to all Kraus operators is the same. The general form of the decomposition of unitary dilations is denoted by U and given below.

$$\begin{aligned}
 U &= {}^1R_{\bar{x}}^{\theta_{17}} \cdot {}^1R_{\bar{y}}^{\theta_{16}} \cdot \text{CNOT}_{31} \cdot {}^1R_{\bar{x}}^{\theta_{15}} \cdot {}^1R_{\bar{y}}^{\theta_{14}} \cdot \text{CNOT}_{21} \cdot {}^1R_{\bar{x}}^{\theta_{13}} \cdot {}^1R_{\bar{y}}^{\theta_{12}} \cdot \text{CNOT}_{31} \cdot {}^1R_{\bar{x}}^{\theta_{11}} \cdot {}^1R_{\bar{y}}^{\theta_{10}} \cdot \text{CNOT}_{21} \cdot {}^1R_{\bar{x}}^{\theta_9} \cdot \\
 &{}^1R_{\bar{y}}^{\theta_8} \cdot \text{CNOT}_{31} \cdot {}^1R_{\bar{x}}^{\theta_7} \cdot {}^1R_{\bar{y}}^{\theta_6} \cdot \text{CNOT}_{31} \cdot {}^1R_{\bar{x}}^{\theta_5} \cdot {}^1R_{\bar{z}}^{\theta_4} \cdot \text{CNOT}_{21} \cdot {}^1R_{\bar{z}}^{\theta_3} \cdot \text{CNOT}_{31} \cdot {}^1R_{\bar{z}}^{\theta_2} \cdot \text{CNOT}_{21} \cdot {}^1R_{\bar{z}}^{\theta_1} \cdot {}^3R_{\bar{z}}^{\theta_0}
 \end{aligned} \tag{B1}$$

where ${}^iR_{\phi}^{\theta}$ represents a single-qubit rotation gate acting on the i th qubit with rotation angle θ and axis of rotation ϕ ; CNOT_{ij} represents a standard two-qubit CNOT gate with i being the control qubit and j being the target qubit.

TABLE V. The values of θ_i s (Eq.B1) required to the implement unitary dilation operators U_{A_j} .

	U_{A_1}	U_{A_2}	U_{A_3}	U_{A_4}
θ_0	1.5708	4.7124	4.7124	1.5708
θ_1	6.2759	0.0486	6.1354	0.1079
θ_2	5.7332	0.0306	0.1041	0.8518
θ_3	0.5359	0.1169	5.7425	5.6472
θ_4	4.2067	1.3599	2.4207	4.9160
θ_5	2.8192	3.0589	3.4918	2.6544
θ_6	1.8641	1.5181	1.2934	1.2327
θ_7	2.2842	1.0045	5.3556	1.0113
θ_8	0.4323	0.0979	0.4432	0.5851
θ_9	3.1416	3.1416	3.1416	3.1416
θ_{10}	0.4323	0.0979	0.4432	0.5851
θ_{11}	2.2856	0.6158	5.0076	3.7509
θ_{12}	1.0560	0.1859	0.6384	1.1481
θ_{13}	2.3100	2.9610	2.8007	5.0366
θ_{14}	0.6701	0.4389	0.9546	1.3207
θ_{15}	1.1972	0.1460	3.6109	4.3664
θ_{16}	1.6675	1.4041	2.5217	1.8259
θ_{17}	2.9373	2.1115	2.4411	3.8623